PCCP

PAPER

View Article Online
View Journal | View Issue

Cite this: *Phys. Chem. Chem. Phys.*, 2019, **21**, 9407

Computational study of the mixed B-site perovskite $SmB_xCo_{1-x}O_{3-d}$ (B = Mn, Fe, Ni, Cu) for next generation solid oxide fuel cell cathodes†

Emilia Olsson, [a] Jonathon Cottom, [b] Xavier Aparicio-Anglès [a] and Nora H. de Leeuw *[ac]

Received 19th February 2019,
Accepted 15th April 2019

DOI: 10.1039/c9cp00995g

rsc.li/pccp

$SmCoO_3$ is a promising perovskite material for the next generation of intermediate temperature solid oxide fuel cells (SOFC), but its potential application is directly linked to, and dependent on, the presence of dopant ions. Doping on the Co-site is suggested to improve the catalytic and electronic properties of this cathode material. Fe, Mn, Ni, and Cu have been proposed as possible dopants and experimental studies have investigated and confirmed the potential of these materials. Here we present a systematic DFT+*U* study focused on the changes in electronic, magnetic, and physical properties with B-site doping of $SmCoO_3$ to allow cathode optimization. It is shown that doping generally leads to distortion in the system, thereby inducing different electron occupations of the Co d-orbitals, altering the electronic and magnetic structure. From these calculations, the 0 K electronic conductivity (σ_e) was obtained, with $SmMn_xCo_{1-x}O_3$ having the highest σ_e, and $SmFe_xCo_{1-x}O_3$ the lowest σ_e, in agreement with experiment. We have also investigated the impact of dopant species and concentration on the oxygen vacancy formation energy (E_f), which is related to the ionic conductivity (σ_O). We found that the E_f values are lowered only when $SmCoO_3$ is doped with Cu or Ni. Finally, thermal expansion coefficients were calculated, with Mn-doping showing the largest decrease at low x and at x = 0.75. Combining these results, it is clear that Mn-doping in the range x = 0.125–0.25 would imbue $SmCoO_3$ with the most favorable properties for IT-SOFC cathode applications.

1. Introduction

Solid oxide fuel cells (SOFC) are low-emission, high efficiency electrical generators, which show great promise as an emerging energy technology.[1–3] However, in order to decrease costs and to prolong cell lifetimes, a concerted research effort is required to lower SOFC operating temperatures into the temperature range 500–800 °C.[1–3] Unfortunately, traditional cathode materials such as $La_xSr_{1-x}MnO_{3-d}$ (LSM), which has long been the state-of-the-art SOFC cathode, have been shown to be inefficient under these operating conditions.[4,5] It is the main task of the cathode to catalyze the oxygen reduction reaction (ORR) and facilitate oxygen diffusion through the electrolyte towards the anode. To this end, it should have high electronic conductivity (σ_e), which depends on the electronic structure, and ionic conductivity (σ_O) which is dependent on the concentration of oxygen vacancies (V_O) and therefore on the oxygen vacancy formation energy (E_f).[1–3,6] The cathode should further be chemically and physically compatible with the coupled electrolyte. Hence, having thermal expansion coefficients (TEC) close to those of traditional electrolytes ($10–13 \times 10^{-6}$ K^{-1}) is important to minimize strain in the cell to prevent premature failure.[7]

In view of the above, new cathode materials are sought, which has led to interest in cobalt-based cathodes.[8] These materials have shown excellent SOFC cathode properties at intermediate temperatures, with high σ_O and σ_e.[8] A promising

[a] *Department of Chemistry, University College London, WC1H 0AJ, London, UK. E-mail: k.olsson.12@ucl.ac.uk*
[b] *Department of Physics and Astronomy, University College London, WC1E 6BT, London, UK*
[c] *School of Chemistry, Cardiff University, Main Building, Park Place, CF10 3AT, Cardiff, UK. E-mail: deleeuwn@cardiff.ac.uk*

† Electronic supplementary information (ESI) available: Summary of the interatomic potential parameters used for the calculation of thermal expansion coefficients (Table S1), a graphical representation of the different magnetic structures investigated in the main article (Fig. S1), a description on how to obtain chemical potential phase diagrams and link this to the oxygen vacancy formation energy; chemical potential phase diagrams for $SmMnO_3$ and $SmFeO_3$ (Fig. S2); a complete list of all the differences in energy between the different dopant configurations in the individual systems (Table S2); the B–O bond lengths for the most stable structures (Table S3); Bader charges for $SmB_xCo_{1-x}O_3$ (Table S4), the magnetic structures calculated for $SmBO_3$ and their relative energies (Table S5); larger DOS (Fig. S3–S7), and electrical conductivities for all systems (Table S6). Additionally, a table with all the oxygen vacancy positions and oxygen vacancy formation energies is included in Table S7, and thermal expansion coefficients in Table S8. See DOI: 10.1039/c9cp00995g

material is $SmCoO_3$, which is in itself a semiconductor, but by doping this perovskite on the Co-site with manganese, nickel, iron, or copper, σ_e can be increased through modification of its electronic structure.[9–12] Such doping makes $SmCoO_3$ a p-type semiconductor, and samarium oxide perovskites doped with transition metals on the B sites, show excellent promise as intermediate temperature (IT-SOFC) cathodes.[13] Fullarton *et al.* discovered that partial substitution on Sm- (with Sr and Ca) and/or Co- (with Ni, Cu, and Fe) sites in $SmCoO_3$ greatly improves σ_O.[14] In combination with doping on the Sm site, substitutional Co-site doping of $SmCoO_3$ with other transition metals has the potential to increase σ_e, by making the materials metallic and magnetic, as well as having an impact on the TEC which decreases.[10,15] For example, Mn-doping of $SmCoO_3$-type cathode materials has been shown experimentally to decrease the TEC, alter the catalytic properties, and increase conduction – property changes that have also been shown for La-based systems.[11] Fe-, Ni- and Cu-doping have been suggested to greatly modify the oxygen diffusion, oxygen surface-to-bulk incorporation, and the catalytic oxygen reduction activity of $SmCoO_3$.[14] Ni-doped $SmCoO_3$ has also been shown experimentally to alter the electronic conduction, and be capable of accommodating oxygen deficiency.[15] Furthermore, Ni-, Fe- and Mn-doping have also been shown to readily reduce the TEC of $SmCoO_3$-based cathode materials.[13,16]

However, the full substitution of Co by dopants leads to completely different types of perovskite materials ($SmBO_3$), which, compared to $LaBO_3$, have been subject to few experimental and only some theoretical studies. Previous computational research has focused on $SmFeO_3$[17–20] and $SmMnO_3$[21,22] whereas computational information on $SmNiO_3$ and $SmCuO_3$ is scarce.[23–27] However, experimental studies exist, providing the basis for this study,[15,28–30] where both Ni and Cu are proposed to readily decrease the TEC in SOFC cathodes, and to be possible dopants in $SmCoO_3$.[14,25]

Taking into account previous work and the promise of $SmCoO_3$ as an IT-SOFC cathode material, here we present a systematic study on the doping of $SmCoO_3$ with Mn, Fe, Ni, and Cu at different concentrations, as well as the fully substituted $SmBO_3$ pseudo-cubic structures. We pay special attention to the effect of the dopant concentrations on the geometric, electronic and magnetic structures, as well as the electronic and ionic conductivities. In addition, the energetics and electronic implications of the oxygen vacancy formation is also investigated. Each of these data points are combined to allow the optimization of properties for B-site doping of $SmCoO_3$.

2. Computational details

2.1 Density functional theory (DFT) calculations

All calculations except for the thermal expansion, discussed below, in this study employed the Vienna ab initio simulation package (VASP, version 5.3.5).[31–34] We have applied the projector-augmented wave method (PAW) to describe the ion–electron interaction,[35] and, based on convergence tests, the energy cut-offs for all systems were set to 500 eV. Spin-polarized calculations were executed using the Perdew–Burke–Ernzerhof (PBE)[36,37] functional under electronic (convergence criterion of 10^{-5} eV) and ionic (convergence criterion of 10^{-3} eV Å^{-1}) self-consistence. The following valence electrons were considered for the atomic species involved: Sm ($5s^2 5p^6 6s^2$), Mn ($3p^6 3d^6 4s^1$), Fe ($3p^6 3d^6 4s^2$), Co ($4s^2 3d^7$), Ni ($4s^2 3d^8$), Cu ($4s^1 3d^{10}$) and O ($2s^2 2p^4$). Furthermore, the tetrahedron method with Blöchl corrections for smearing[38] was applied, together with a $4 \times 4 \times 4$ Γ-centered Monkhorst–Pack grid.[39] Bader AIM (Atoms in Molecules) charges[40] were calculated using the Henkelman algorithm.[41] The supercell used throughout this work is the $2 \times 2 \times 2$ $Pm\bar{3}m$ pseudo-cubic cell, as this was found to be large enough to model bulk properties and defect structures within reasonable computational resources.

To describe electronic structures, we have used the on-site coulombic interaction (DFT+U) for the B 3d-electrons. Normal exchange correlation functionals (LDA or GGA) cannot correct the electron self-interaction problem, leading to a metallic description of perovskites or at least an underestimation of their band gaps.[42–44] In this work, we have employed Dudarev's approach,[45] in which an effective Hubbard parameter (U_{eff}) is applied to the B d-states. The U_{eff}-parameters for B ions in perovskites have been extensively fitted and tested elsewhere, based on lattice parameters, band gaps and properties such as magnetic structures, enthalpy of formation, and defect formation energies. Based on this prior work, here we have used the following Hubbard parameters: U_{eff} = 4 eV[46] for Mn, U_{eff} = 4.3 eV[47] for Fe, U_{eff} = 3 eV[48] for Co, U_{eff} = 6.4 eV[46] for Ni, and U_{eff} = 3 eV[49] for Cu. The electronic conductivity is calculated for the 0 K optimized electronic structures from the frequency dependent dielectric matrix, where the electronic conductivity can be calculated from the dielectric constant, dielectric loss factor, and the loss tangent, which are then obtained from the dielectric parameters.[50–53]

2.2 Molecular dynamics (MD) simulations

Thermal expansion coefficients were calculated from molecular dynamics (MD) simulations using the DL_POLY 4 program.[54] $20 \times 20 \times 20$ supercells based on the DFT+U optimized $SmB_xCo_{1-x}O_3$ structures were simulated under *NPT* conditions (constant number of particles, pressure and temperature), with a Nosé–Hoover thermostat.[55] All statistics were collected after a 10 ps system equilibration, with a 100 ps production phase and a time step of 0.1 fs. To account for electrostatic interactions, the Ewald summation was employed, and the Verlet algorithm was employed to evaluate the atomic motions. Short-range atomic interactions were calculated with Buckingham potentials (eqn (1)), which are used extensively within the Born model for ionic solids.[56–58] Eqn (1) shows the Buckingham potential expression, with r defining the distance between ions i and j, and A, ρ, and C being empirically fitted parameters.

$$V_{i,j}(r) = A \exp\left(\frac{-r}{\rho}\right) - \frac{C}{r^6} \quad (1)$$

To describe the electronic polarization of the atoms (α), the shell model is included,[48,59] where ions are modelled as cores,

connected by a harmonic spring (k) to a massless shell with charge Y (eqn (2)).

$$\alpha = \frac{Y^2}{k} \quad (2)$$

The relevant interatomic potentials are taken from the Cherry *et al.* library, as these have previously been used to model σ_O in perovskites,[60] and have already been evaluated for $SmCoO_3$.[61] The full set of interatomic potentials is presented in Table S1 in the ESI.†

3. Results and discussion

3.1 Dopant configuration

As a first step, the non-equivalent dopant configurations in $SmB_xCo_{1-x}O_3$ were evaluated using the Site-Occupancy Disorder Program (SOD).[62] The $2 \times 2 \times 2$ supercell includes eight Co lattice positions, thus a substitution of one Co by a dopant ion B represents a dopant concentration of $x = 0.125$ (for which only one non-equivalent structure can be found), for two Co substitutions $x = 0.25$, four substitutions $x = 0.50$, and finally in $x = 0.75$ we have two Co and six B. Three inequivalent configurations exist for $x = 0.25$ and 0.75, and six for $x = 0.5$. The different $SmB_xCo_{1-x}O_3$ configurations were optimized with VASP, with their relative energies collected in Table S2 of the ESI,† after which the lowest energy configurations were selected for further study (Fig. 1). In real systems, a degree of disorder between dopant configurations would be expected. However, in order to avoid confusion, and as the smallest energy difference between the different dopant configurations for any particular dopant and dopant level was more than 0.1 eV, only the lowest energy configurations have been considered here. It was found that the lowest energy dopant configurations were dependent on both the dopant type and dopant configuration.

In order to further understand the trends in doped $SmB_xCo_{1-x}O_3$, we have also studied the $SmBO_3$ perovskites. Cubic $SmBO_3$ perovskites are isostructural, with differences in the B–O bond lengths ranging from 0 to 0.6 Å related to the differences in B ionic radii between the materials (Table S3 in ESI†). As a result, variations in lattice parameter are observed over the periodic series (Table 1), according to the nature of B, in terms of ionic radii and electronegativity, which will influence the chemistry and physical properties of these materials.

3.2 Electronic and magnetic structures

Co and B can exist in different spin states, depending on the d-orbital occupation. Co^{3+} ($3d^6$) has a low-spin ground state (LS, $t_{2g}^6e_g^0$), and a negligible magnetic moment (μ) of 0 μ_B.[63] However, upon distortion of the CoO_6-octahedra, the d-orbital occupation can be altered, resulting in different spin states, specifically intermediate (IS, $t_{2g}^5e_g^1$) or high (HS, $t_{2g}^4e_g^2$) states, thus modifying the magnetic properties of the system.[48,64] In addition, the dopants considered in this work can also present different d-orbital occupations and consequently different spin states.[46,65]

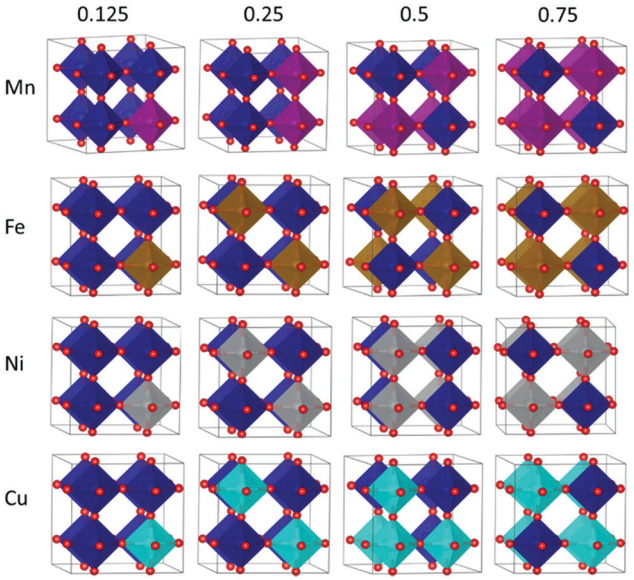

Fig. 1 Polyhedral representation of the lowest energy dopant configurations. First row is B = Mn (purple), second row B = Fe (brown), third row B = Ni (grey), and fourth row B = Cu (turquoise), with Co represented in dark blue, and red spheres are O. Sm has been omitted for clarity. Columns represent the concentrations from left to right $x = 0.125$, $x = 0.25$, $x = 0.5$ and $x = 0.75$.

The spin arrangement is important as it determines the magnetic structure of the material. Three general magnetic structures are possible: non-magnetic (NM), antiferromagnetic (AFM), and ferromagnetic (FM). Additionally, AFM can be presented in different configurations: C-type, A-type, and G-type, all schematically represented in Fig. S1 (ESI†). We evaluated all the potential magnetic structures for all dopants and concentrations. Interestingly, almost all $SmB_xCo_{1-x}O_3$ compositions were calculated to have a FM structure, whereas we could not obtain either AFM or NM structures. However, there were two exceptions; $SmCu_{0.5}Co_{0.5}O_3$ and $SmCu_{0.75}Co_{0.25}O_3$ converged for the G-AFM structure, indicating a clear preference by this type of system for the ferromagnetic structure (Table 1). We were also able to converge different magnetic structures for pure $SmBO_3$, whose relative energies can be found in Table S5 of the ESI.† $SmFeO_3$ was found to have a C-AFM ground state, with G-AFM being the energetically second-most stable configuration, found to be 0.11 eV per formula unit higher in energy. For $SmMnO_3$ and $SmNiO_3$, FM configurations are more stable than AFM, where in both cases the difference in energy to the second-most stable magnetic structure was more than 0.4 eV per formula unit, in agreement with previous data on cubic phase lanthanide manganate perovskites, and cubic $SmNiO_3$ (which undergoes an insulator-to-metal transition at $\sim$400 K).[15,66] Finally, for $SmCuO_3$, our calculations could only obtain the FM and NM structures, and, according to their relative energies, this material is expected to be non-magnetic, with the FM structure 0.66 eV per formula unit higher in energy.

For $SmMn_xCo_{1-x}O_3$, regardless of the dopant concentration, an overlap between the Co and Mn e_g-bands (Fig. 2) is always found at the Fermi level, anticipating a high electron conductivity,

Table 1 Lattice parameter (a) in Å, local magnetic moments (μ) in μ_B for cobalt and dopant, band gap (E_g) in eV, and magnetic ordering in $SmB_xCo_{1-x}O_3$. The magnetic moments of samarium and oxygen were found to be negligible in relation to the transition state metals. a for $SmCoO_3$ is 3.75 Å, q_{Co} in $SmCoO_3$ is 1.31 e.[48,64] A full list of Bader charges for each system is included in Table S4 in the ESI

B		x = 0.125	x = 0.25	x = 0.5	x = 0.75	x = 1.0
Mn	a	3.76	3.78	3.83	3.85	3.87 (3.89)[22]
	μ_{Mn}	3.4	3.5	3.5	3.8	3.9
	μ_{Co}	0.2, 0.06	0.2	2.4, 0.4	0.4	
		FM	FM	FM	FM	FM
	q_{Mn}	1.74	1.74	1.70	1.68	1.71
	q_{Co}	1.28	1.25	1.14, 1.35	1.13	
	E_g	0.78 (α), 0 (β)	0 (α), 0.97 (β)	0 (α), 1.66 (β)	0 (α), 2.16 (β)	0.0 (α), 2.90 (β)
Fe	a	3.78	3.78	3.81	3.85	3.89
	μ_{Fe}	4.2	4.2	4.2	4.3	4.2
	μ_{Co}	0.0, 0.2	0.2	0.3	0.4	
		FM	FM	FM	FM	CAFM
	q_{Fe}	1.70	1.73	1.71	1.68	1.61
	q_{Co}	1.28	1.26	1.17	1.18	
	E_g	0.18 (α), 0.48 (β)	0.46 (α), 0 (β)	2.23 (α), 1.67 (β)	1.04 (α), 1.69 (β)	2.16
Ni	a	3.77	3.81	3.77	3.77	3.78 (3.81)[23]
	μ_{Ni}	1.7	1.7	1.6	1.7, 0.9, 1.6	1.3
	μ_{Co}	0.5, 0.7, 2.9, 3.0	0.01, 1.7, 1.8	1.5	1.3	
		FM	FM	FM	FM	FM
	q_{Ni}	1.17	1.29	1.27	1.33, 1.12	1.21
	q_{Co}	1.17, 1.55	1.21, 1.36	1.35	1.31	
	E_g	1.49 (α), 0 (β)	0 (α), 0.40 (β)	1.12 (α), 0 (β)	0 (α), 1.22 (β)	0.0(α), 2.25 (β)
Cu	a	3.76	3.81	3.80	3.81	3.80
	μ_{Cu}	0.8	0.7	0.6	2.6, 0.7	0.0
	μ_{Co}	0.1, 0.0	1.1, 0.4, 3.0	1.3	0.6	
		FM	FM	GAFM	GAFM	NM
	q_{Cu}	1.32	1.28	1.25	1.18, 1.20	1.15
	q_{Co}	1.30	1.19, 1.30, 1.53	1.34, 1.24	1.40	
	E_g	0.66 (α), 0 (β)	1.02 (α), 0 (β)	0 (α), 0.67 (β)	0.06 (α), 0.21 (β)	0.0

as high σ_e has been reported to go through e_g-bands.[67,68] The contribution of each band depends on the dopant concentration, with larger contributions of the Co e_g-bands at lower dopant concentrations, and *vice versa* when the material is heavily doped. Increasing the dopant concentration does not affect the Co t_{2g}/e_g-splitting. We know from previous publications that the change in the spin state, and thus the occupation of the d-orbitals in Co, can be directly related to the distortion of the octahedral environment, *i.e.* distortions in the Co–O bonds.[64] Indeed, for x = 0.125, x = 0.25 and x = 0.75, these bonds are only distorted by ≈0.01 Å with respect to the ideal Co–O bond of 1.88 Å. However, for x = 0.50, the range of Co–O bond lengths is wider (1.88–1.95 Å), thus altering the Co d-orbital crystal field splitting, and consequently, the orbital occupation.

This exception for x = 0.5 can also be observed in the variation of the cobalt magnetic moment. As shown in Table 1, μ_{Co} is close to 0 for all concentrations, with the exception of x = 0.50 with a μ_{Co} of 2.4 that can be associated to an intermediate spin (IS) state. This behavior is also observed in the PDOS, with the occupation of the Co e_g-orbitals on the one hand and β-t_{2g}-orbitals at positive energies on the other. Moving through the PDOS with increasing x, it can be seen that this material becomes gradually more like $SmMnO_3$. The β-band gap increases with increasing x, reaching a maximum in $SmMnO_3$. Also noticeable is the magnetic moment of Mn, which is found to be between 3.76 and 3.85, indicating that Mn is found in its higher spin state, with the highest Mn magnetic moment observed in $SmMnO_3$. Furthermore, μ_{Mn} decreases with decreasing Mn-content (x_{Mn}), a behaviour that has been observed previously in $LaMn_{1-x}CoO_3$.[69]

The crystal field splitting for cobalt is further observed to remain unchanged with increasing Fe concentration (Fig. 2), which is mainly due to the low degree of distortion suffered by the Co–O bonds upon Fe-doping, as can be seen in Table S3 of the ESI.† At x = 0.125, Fe-doped $SmCoO_3$ is metallic, with an overlap of Fe e_g- and Co t_{2g}-bands at the Fermi level, where we thus may expect a relatively large electronic conductivity. However, with increasing dopant concentration, the material becomes increasingly semiconducting, disqualifying it as a good cathode candidate. As was observed for $SmMn_xCo_{1-x}O_3$, $SmFe_xCo_{1-x}O_3$ gains more $SmFeO_3$ character with increasing x, with the band gap becoming increasingly symmetrical, resulting in pure semi-conductor behaviour at x = 1.0. On the other hand, the iron magnetic moment remains mostly constant over the series at 4.2 μ_B, whereas the Co magnetic moments are very low for the entire series, oscillating between 0.0 and 0.4 μ_B. In $SmFeO_3$, all Fe–O bond lengths are equal, which results in a symmetrical electronic structure. It is worth noting that all Fe–O bonds are equal for x = 0.5 as well, but the Co–O bond lengths, whilst all the same, are different to the Fe–O bonds, thus inducing distortions in the oxygen sublattice resulting in an asymmetric PDOS.

The electronic structures of $SmNi_xCo_{1-x}O_3$ and $SmCu_xCo_{1-x}O_3$ show different behaviour to the Fe- and Mn-doped systems.

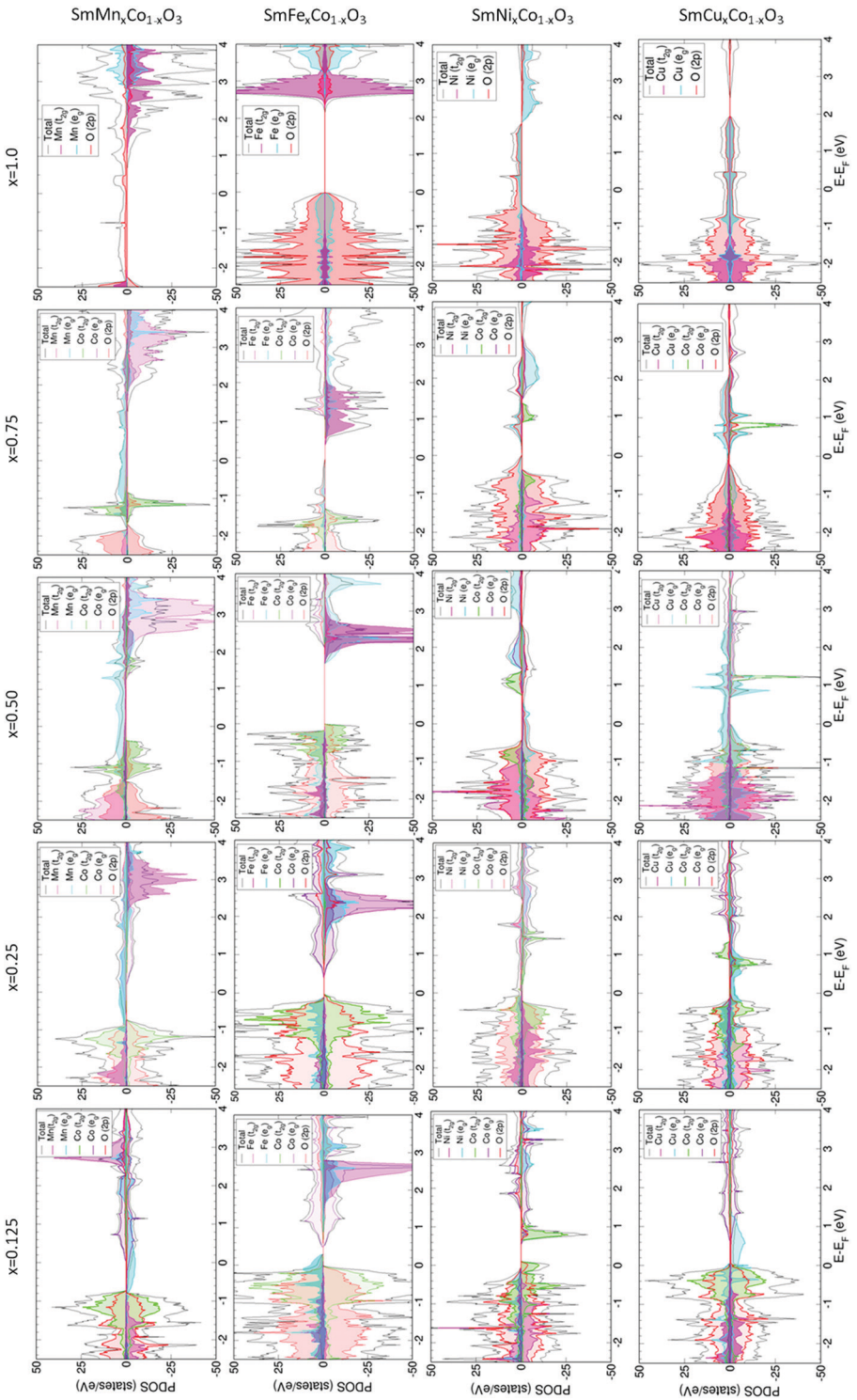

Fig. 2 Projected density of states (PDOS) for $SmB_xCo_{1-x}O_3$. The Fermi level is at 0 eV for all representations, where negative values represent the occupied bands and positive values represent the virtual bands. In addition, positive PDOS are associated to the α-spin whereas negative PDOS are associated to β-spin. Note that the Mn, Fe, Ni, and Cu PDOS have been multiplied by a factor of 10 for x = 0.125, 5 for x = 0.25, 0.5, and by 2 for x = 0.75.

In $SmNi_xCo_{1-x}O_3$, the Co t_{2g}-bands are not fully occupied whereas the e_g-bands are partially occupied, which can be related directly to a change in the Co spin moment, and thus to the changes in the Co–O distances (Table S3, ESI†). Interestingly, for x = 0.125 the system is a conductor, but conduction occurs only through the Co t_{2g}-bands and as soon as the dopant concentration increases, the system becomes half-metallic and the conduction occurs through the nickel e_g-bands. The half-metallic nature is preserved in $SmNiO_3$, thus inferring that Ni-doping, even at low concentrations, induces

more $SmNiO_3$-type behavior than $SmCoO_3$-type. It is worth noting that there is no overlap between the bands of Co and Ni, which is indicative of poor electronic conductivity.

For $SmCu_xCo_{1-x}O_3$ (Fig. 2), the Cu e_g-bands are partially occupied over the Fermi level for $x = 0.125$, $x = 0.25$ and $x = 0.5$, indicating that electronic conductivity should be possible. For $x = 0.75$, a change in the electronic structure is seen around the Fermi level, resulting in a small band gap, which would suggest a decrease in σ_e. For $SmCuO_3$, the electronic structure becomes fully metallic and ferromagnetic. Additionally, for all x_{Cu}, the cobalt octahedral environment is distorted, resulting in the Co t_{2g}-levels splitting over the valence and conduction bands, which again can be related directly to a change in the cobalt spin moment, and thus to distortions in the Co–O distances, as listed in Table S3 (ESI†).

Moreover, Bader charges and magnetic moments for cobalt at different concentrations suggest the presence of different mixed valence states, for example when $x = 0.125$. In this situation, Co charges decrease and increase by ~ 0.2 e with respect to the Co charge in $SmCoO_3$. This difference could be seen as a partial change in oxidation state, but neither the magnetic moments nor the electronic structure are clear enough to support this idea. On the other hand, nickel's magnetic moment is around 1.7 for all concentrations, indicating that nickel is found in a mixed spin state.

3.2.1 Electronic conductivity (σ_e). It is generally accepted for SOFC cathodes that a high electronic conductivity (σ_e) is required for good cathode performance.[70] Here, we have calculated the electronic conductivities for all the aforementioned $SmB_xCo_{1-x}O_3$ at 0 K (Table S6 in ESI† and Fig. 3). Although thermal effects may alter the electronic conduction, as we strive to study relevant trends due to dopant effects, the 0 K electronic conduction is a suitable first approximation. From these results, it is clear that in $SmFe_xCo_{1-x}O_3$ $\sigma_e = 0$ S cm^{-1} for $x > 0.125$, as expected considering that the PDOS revealed that the material becomes semi-conducting. It is known from experimental data that Fe-containing perovskites generally have lower σ_e than those containing manganese,[71,72] and that $\sigma_e \neq 0$ S cm^{-1} in Fe-based perovskites at temperatures above 200 °C.[10,71] Thus, it is reasonable to suggest that at elevated temperatures, σ_e will increase for this material,[71,73] although this increase in σ_e is not expected to be remarkable in comparison to the other systems modelled here. Focusing on those systems with the highest σ_e, *i.e.* $SmMn_{0.125}Co_{0.875}O_3$, $SmMn_{0.25}Co_{0.75}O_3$, $SmFe_{0.125}Co_{0.875}O_3$, and $SmNi_{0.25}Co_{0.75}O_3$, it is seen that Cu-doping would not represent a major improvement in terms of σ_e since the maximum σ_e that can be obtained is at $x = 0.25$ with a σ_e of 120 S cm^{-1}.

The largest σ_e are obtained for $SmMn_{0.125}Co_{0.875}O_3$, and $SmFe_{0.125}Co_{0.875}O_3$. These large σ_e can be attributed to the overlapping between the d-bands of Co and the dopants.[74,75] It is further expected that at higher temperatures, these σ_e could be increased. Moreover, all σ_e are in line with general IT-SOFC cathode requirements and experimentally obtained data.[10,70,71,76]

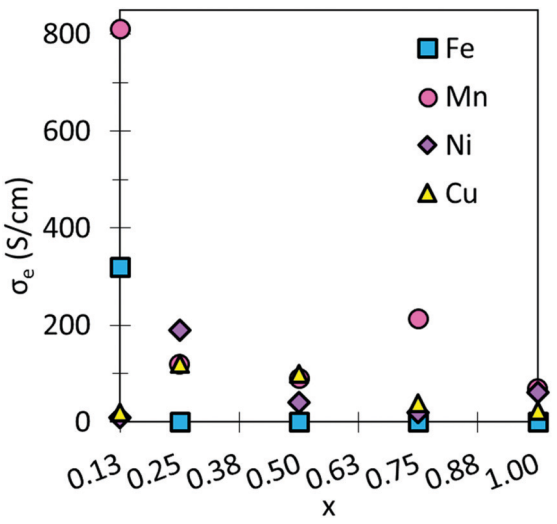

Fig. 3 σ_e (S cm^{-1}) as a function of x for $SmB_xCo_{1-x}O_3$.

3.3 Hole and oxygen vacancy formation

A critical property for SOFC cathodes is their high combined electronic and ionic conductivity. Mixed ionic and electronic conductors (MIECs) have electronic conductivity (as presented above) reinforced by ionic conductivity. Ionic conductivity in these perovskites proceeds *via* an oxygen vacancy hopping mechanism, inferring that a high concentration of oxygen vacancies is important. Oxygen vacancies are generally formed as the result charge compensation, but can also be formed as a function of oxygen partial pressure and temperature. Furthermore, it has been demonstrated that hole formation could lead to higher electronic conductivity.[72,77] Hence, we below investigate both hole and oxygen vacancy formation in $SmB_xCo_{1-x}O_3$.

3.3.1 Hole formation. Perovskite oxides are known to be able to accommodate hole polarons, which have been identified in other perovskites such as $SrTiO_3$, and manganese in particular is known to be prone to form electron–hole pairs.[72,78] Hole formation energies can be calculated as the difference in total energy between the fully relaxed localized polaron state, and the delocalized hole state in the undistorted lattice. Using this formulation, a large negative hole formation energy indicates that the relaxed structure is more energetically stable than the unrelaxed hole. Hence, the energetic difference represents the energy gained on hole localization, shown in Table 2.

Examining Table 2, we can see that the hole formation energies as a result of Ni- and Cu-doping are quite high, with similar energies seen for Fe-doping at $x = 0.125$, and 0.75.

Table 2 Hole formation energies (eV) for $SmB_xCo_{1-x}O_3$

B	$x = 0.125$	$x = 0.25$	$x = 0.5$	$x = 0.75$
Mn	−0.13	−0.23	−0.47	−0.15
Fe	−1.28	−0.27	−0.40	−1.39
Ni	−0.66	−1.03	−1.27	−1.07
Cu	−1.12	−0.79	−1.02	−0.13

Hence, the hole polarons formed in these systems represent the deep hole states that would be expected to remain localized at device operating temperatures. Mn-doping on the other hand leads to much smaller hole formation energies, which is in line with previous work on manganese-based perovskites.[72] The hole formation in Mn-containing systems has been assigned to the breakdown of the Mn^{3+} charge state to Mn^{2+} and Mn^{4+}, which furthermore leads to high electronic conductivity as these states are shallow and hence mobile at elevated temperatures.[72]

3.3.2 Oxygen vacancy formation. Oxygen vacancies influence the bulk ionic conduction in SOFC cathode materials, and thus it is important to assess the effect of the dopants on the oxygen vacancy formation. The SOD program[62] was utilized to introduce a single oxygen vacancy (V_O) in all systems, and the models were then optimized using VASP. The oxygen vacancy formation energy (E_f),[79] with lower E_f indicating higher V_O concentration (C_V) at equilibrium conditions,[48] is calculated according to eqn (3) and (4),

$$E_f = E_{Defective} - E_{Bulk} + \mu_O \quad (3)$$

$$\Delta\mu_O = \mu_O - \frac{1}{2}g^{tot}_{O_2} \leq 0 \quad (4)$$

where k_B is the Boltzmann constant, T the temperature, $E_{Defective}$ the total energy of the system with V_O, E_{bulk} the total energy of the bulk, and μ_O is the oxygen chemical potential.[80–85] $\Delta\mu_O$ is the oxygen chemical potential deviation, and $g^{tot}_{O_2}$ is the free energy of the oxygen molecule ($O_{2(g)}$).[80–85] It is widely accepted that $g^{tot}_{O_2}$ can be approximated by the DFT energy of $O_{2(g)}$ (E_{O_2}) when calculations are performed under oxygen-rich conditions, and the material is in thermodynamic equilibrium with the surface, and that the latter is in equilibrium with the gas phase.[83] However, it is necessary to determine first whether the material is stable or not for $\Delta\mu_O = 0$, which is evaluated through chemical potential phase diagrams. A more detailed explanation on how to construct these diagrams can be found in the ESI.†

3.3.2.1 Oxygen vacancy formation in $SmB_{1-x}Co_xO_3$. For $SmCoO_3$, it was shown in our previous work that the upper limit to $\Delta\mu_O$ is −0.5 eV.[48] In this work, we thus constructed phase diagrams for $SmMnO_3$ and $SmFeO_3$, from which we found that the upper limits of the oxygen potential (eqn (4)) for $SmMnO_3$ (based on experimental data from Pawlas-Foryst *et al.*[86]) is $\Delta\mu_O \leq 0$ eV, whereas for $SmFeO_3$ (based on experimental data from Parida *et al.*[87]) it is $\Delta\mu_O \leq -0.7$ eV. The lack of experimental data for $SmCuO_3$ and $SmNiO_3$ meant that we could not calculate their respective phase diagrams, although it has been reported that both materials are unstable under high partial oxygen pressures.[24,26,27]

As such, for ease of comparison $\Delta\mu_O = -0.5$ eV has been used for all materials and concentrations, and we have assumed that the ensuing error for $SmFeO_3$ is negligible for the purpose of this discussion.[13,48] However, we have considered $\Delta\mu_O = 0$ for $SmMn_{0.75}Co_{0.25}O_{3-x}$, since its stoichiometry is closer to $SmMnO_3$ than it is to $SmCoO_3$.

Table 3 Lowest E_f (eV) for $SmB_xCo_{1-x}O_3$. For vacancy position and a complete list of E_f, please see Table S7 in the ESI

B	x = 0.125	x = 0.25	x = 0.5	x = 0.75	x = 1.0
Mn	1.77	1.85	2.06	2.20	2.36
Fe	1.82	2.20	3.03	1.49	5.65
Ni	1.66	1.09	2.15	0.44	0.55
Cu	1.69	0.55	0.79	0.42	0.54

Comparing the oxygen vacancy formation energies with respect to undoped $SmCoO_3$ (2.08 eV), Co-site doping with B does not markedly lower E_f, except when doped with Cu, and at $x_{Ni} > 0.75$. The calculated oxygen vacancy formation energies for Ni- and Cu-doped $SmCoO_3$ (Table 3, and Table S7 in ESI†) indicate – in agreement with experimental studies[15,24,26,27] – that only $SmNi_xCo_{1-x}O_{3-d}$ and $SmCu_xCo_{1-x}O_{3-d}$ lead to meaningful reduction in the V_O formation energy at higher dopant concentrations. As such, these systems are expected to be oxygen-deficient at IT-SOFC operating temperatures and oxygen partial pressures. However, the effect of Co-site doping on the V_O formation energies is limited when compared to Sm-site doping, where spontaneous formation of oxygen vacancies are observed. Sm-site doping reduces the oxygen vacancy formation energy by more than 2.5 eV,[61] whereas the maximum reduction in oxygen vacancy formation energy seen here is 1.66 eV. Hence, this doping scheme has a much larger effect on the electrical conductivity than the ionic conductivity. This finding is in accordance with B-site doping having a limited effect on σ_O, with a much larger impact seen from Sm-site doping.

3.3.2.2 Oxygen vacancy formation in $SmBO_3$. Comparison of E_f in $SmBO_3$ is presented in Fig. 4. $SmBO_3$ show a non-linear E_f trend (comparable to $LaBO_3$),[6,46] with Fe-based lanthanide oxides having the highest E_f. What is notable in comparison with $LaBO_3$,[6,46] is that the trend is more extreme, where E_f for $SmFeO_3$ is higher by ∼1 eV, whereas E_f for $SmMnO_3$ and

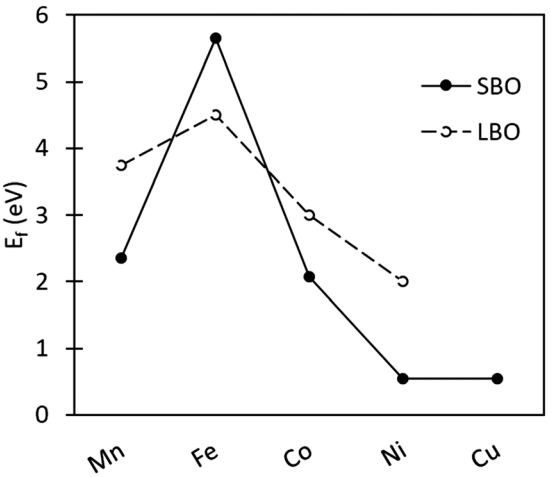

Fig. 4 Oxygen vacancy formation energy as a function of transition metal ion in $SmBO_3$ (B = Mn, Fe, Co, Ni, and Cu). Solid line SBO is $SmBO_3$, and dashed line LBO is $LaBO_3$ with the values taken from Lee *et al.*[46]

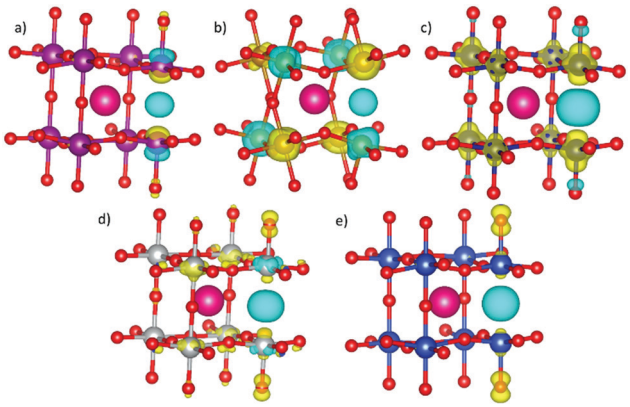

Fig. 5 Representations of the spin density difference ($\Delta\rho^{\alpha-\beta}$) in (a) $SmMnO_3$, (b) $SmFeO_3$, (c) $SmCoO_3$, (d) $SmNiO_3$ and (e) $SmCuO_3$ with V_O. Red spheres are O, purple Mn, pink Sm, orange Fe, dark blue Co, silver Ni, and blue Cu. Yellow $\Delta\rho^{\alpha-\beta}$ iso-surface shows an increase of spin density, whereas blue $\Delta\rho$ iso-surface represents a spin density decrease. Iso-surface value is set at 0.03 e $Bohr^{-3}$. Only one Sm has been included in each representation for clarity.

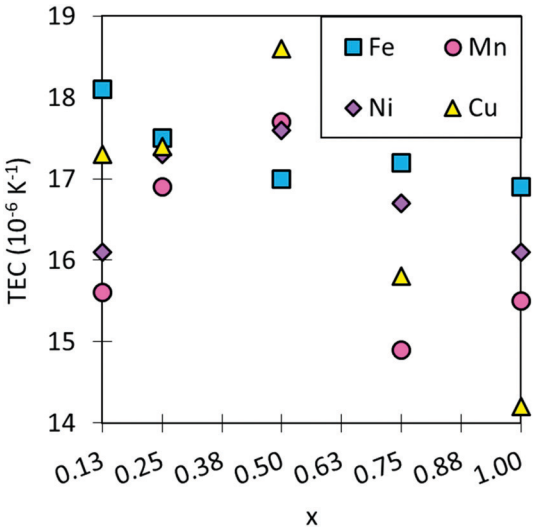

Fig. 6 The trend in TEC for $SmB_xCo_{1-x}O_3$ calculated over a temperature range of 600–1200 K. TECs for typical SOFC electrolytes are ~10–13 × 10^{-6} K^{-1}, which is outside the range of this graph.

$SmCoO_3$ is lower. E_f in $SmNiO_3$ and $SmCuO_3$ are very low, as was also seen for $SmCu/Ni_xCo_{1-x}O_3$. These low E_f are a consequence of the instability of the Ni and Cu 3+ oxidation state, as was observed previously in $LaNiO_3$ and $LaCuO_3$.[88]

To investigate the impact of V_O formation on the charge distribution in $SmBO_3$, we have plotted the change in spin density ($\Delta\rho^{\alpha-\beta}$) upon V_O formation (Fig. 5) as

$$\Delta\rho^{\alpha-\beta} = \rho^{\alpha-\beta}_{SmBO_{3-x}} - \rho^{\alpha-\beta}_{SmBO_3} - \rho^{\alpha-\beta}_{O}$$

$\Delta\rho^{\alpha-\beta}$ shows clearly that in all $SmBO_3$, apart from $SmFeO_3$, B^{2+}–V_O–B^{2+} clusters are formed, indicated from the gain in $\Delta\rho^{\alpha-\beta}$ on the B-sites. This is most clearly evident in $SmMnO_3$, whereas in $SmNiO_3$ and $SmCuO_3$ some additional $\Delta\rho^{\alpha-\beta}$ is located on the oxygen (in the same plane as V_O) nearest to the reduced copper and nickel ions. In $SmFeO_3$, which is the compound that stands out most in this series with the highest E_f, the C-AFM structure is kept, whereas the lattice is distorted, and there is a general change in spin throughout all Fe-sites. The magnetic moments and Bader charges on the neighboring Fe ions have been reduced from μ_{Fe} = 4.2 to $\mu_{Fe\,NN\,V_O}$ = 1.16 and 2.1, which is compatible with iron going from a d^5-occupancy (Fe^{3+}) to d^4 (Fe^{2+}). This change in iron d-occupancy is unfavorable and has been suggested previously to cause the high E_f in $LaFeO_3$.[89] A thorough discussion on V_O formation in $SmCoO_3$ has been presented in a previous publication[48] and is thus only briefly mentioned here.

3.4 Thermal expansion coefficient (TEC)

The TECs of traditional electrolyte materials are in the region of ~10–13 × 10^{-6} K^{-1} and $SmCoO_3$ has a calculated TEC of 17.7 × 10^{-6} K^{-1}. These high TECs are commonplace for cobalt perovskites, and they are known to increase with Sm-site doping, as this increases oxygen deficiency in the lattice, leading to further lattice volume expansion upon heating. Co-site doping can decrease TEC, as seen in Fig. 6 and Table S8 (ESI†), which would make the materials more practical as SOFC cathodes, making the electrolyte and cathode compatible. Encouragingly, most systems investigated here do show lowered TEC compared to $SmCoO_3$, although none are directly in the range of common SOFC electrolytes. As such, none of the materials are suitable as SOFC cathodes in their current compositions. Mn-doping is seen to decrease TEC the most, but it also varies greatly with x. On the other hand, Fe-doping barely affects the TEC at any x. Doping with copper shows no significant change in TEC at low x, but it increases for x = 0.5. Finally, Ni-doping shows similar behaviour to Mn-doping, but does not reduce TEC as readily. Although these results are generally positive in terms of lowering TEC, they are not sufficient to match an acceptable TEC range.

4. Conclusion

In this paper we have presented a detailed atomic-level computational study of $SmB_xCo_{1-x}O_3$ materials, where B = Fe, Mn, Ni, and Cu, and x = 0.125, 0.25, 0.5, 0.75 and 1.00. After a complete study of the dopant configurations, the most stable dopant distributions and concentrations were determined, from which the electronic and magnetic properties, hole formation, oxygen vacancy formation energies, and thermal expansion coefficients were calculated.

Regardless of the dopant, doping on the Co-site induces a distortion of the Co–O bond that forces different Co d-orbital occupations. This effect, in combination with the d-orbital occupation of the dopants, explains why the majority of the systems become ferromagnetic, with the exception of $SmCu_{0.5}Co_{0.5}O_3$ and $SmCu_{0.75}Co_{0.25}O_3$. The overlap between the e_g-orbitals of the dopant and cobalt around the Fermi level explains the impressively high electrical conductivity found for $SmMn_{0.125}Co_{0.875}O_3$ compared to $SmFe_{0.125}Co_{0.875}O_3$, where the presence of an electronic band explains the insignificant

calculated electronic conductivity. We have also illustrated that doping with Cu and Ni does not significantly improve the electronic conductivity of the perovskite. Hence, only Mn-doping would be beneficial for this material as an SOFC cathode, as electronic conductivity is of vital importance for intermediate temperature SOFC cathodes.

Furthermore, B-site doping was not found to reduce significantly the oxygen vacancy formation energy when B = Mn or Fe, but it does decrease with B = Cu or Ni. In general, the most common V_O configuration was found to be Co–V_O–Co, with the reduction of cobalt. Finally, TECs were calculated, where Mn-doping showed the largest decrease at low x. Thus, from the results obtained from the combination of our DFT calculations and MD simulations, we conclude that $SmMn_xCo_{1-x}O_3$ at $x = 0.125$ or $x = 0.25$ would be the most favorable composition to improve $SmCoO_3$ as an IT-SOFC cathode material, but that doping with Fe would be disadvantageous due to the low electronic conductivity. However, to realize the potential of doped $SmCoO_3$ as a SOFC cathode material, studies would need to be conducted combining both the Co-site doping studied here with Sm-doping.

Conflicts of interest

There are no conflicts to declare.

Acknowledgements

The authors acknowledge the Engineering and Physical Sciences Research Council (EPSRC) for financial support (Grants references EP/K016288/1 and EP/K001329/1). We also acknowledge the use of the UCL Legion High Performance Computing Facility (Legion@UCL) and the UCL Grace High Performance Computing Facility (Grace@UCL), and associated support services, in the completion of this work. Finally, *via* our membership of the UK's HPC Materials Chemistry Consortium, which is funded by EPSRC (EP/L000202), this work made use of the facilities of ARCHER, the UK's national high-performance computing service, which is funded by the Office of Science and Technology through EPSRC's High End Computing Programme. DL_POLY_4 has been obtained from STFC's Daresbury Laboratory *via* the website http://www.ccp5.ac.uk/DL_POLY. We acknowledge use of STFC Hartree Centre resources in this work. The STFC Hartree Centre is a research collaboratory in association with IBM providing High Performance Computing platforms funded by the UK's investment in e-Infrastructure. E. O. gratefully acknowledges EPSRC funding from the UCL Centre for Doctoral Training in Molecular Modelling and Materials Science (EP/G036675/1).

References

1 W. C. Chueh and S. M. Haile, Electrochemistry of mixed oxygen ion and electron conducting electrodes in solid electrolyte cells, *Annu. Rev. Chem. Biomol. Eng.*, 2012, **3**, 313–341.
2 S. M. Haile, Fuel cell materials and components, *Acta Mater.*, 2003, **51**, 5981–6000.
3 B. C. Steele and A. Heinzel, Materials for fuel-cell technologies, *Nature*, 2001, **414**, 345–352.
4 R. M. Ormerod, Solid oxide fuel cells, *Chem. Soc. Rev.*, 2003, **32**, 17–28.
5 J. Van Herle, A. J. J. McEvoy and K. Ravindranathan Thampi, A study on the $La_{1-x}Sr_xMnO_3$ oxygen cathode, *Electrochim. Acta*, 1996, **41**, 1447–1454.
6 M. Pavone, A. M. Ritzmann and E. A. Carter, Quantum-mechanics-based design principles for solid oxide fuel cell cathode materials, *Energy Environ. Sci.*, 2011, **4**, 4933.
7 J. A. Kilner and M. Burriel, Materials for Intermediate-Temperature Solid-Oxide Fuel Cells, *Annu. Rev. Mater. Res.*, 2014, **44**, 365–393.
8 X. Jiang, Q. Xu, Y. Shi, X. Li, W. Zhou, H. Xu and Q. Zhang, Synthesis and properties of Sm^{3+}-deficient $Sm_{1-x}BaCo_2O_{5+\delta}$ perovskite oxides as cathode materials, *Int. J. Hydrogen Energy*, 2014, **39**, 10817–10823.
9 J. H. Kim, S.-W. Baek, C. Lee, K. Park and J. Bae, Performance analysis of cobalt-based cathode materials for solid oxide fuel cell, *Solid State Ionics*, 2008, **179**, 1490–1496.
10 K. H. Jung, S. Choi, H.-H. Park and W.-S. Seo, High temperature thermoelectric properties of Sr and Fe doped $SmCoO_3$ perovskite structure, *Curr. Appl. Phys.*, 2011, **11**, S260–S265.
11 Y. Wang, X. Zhao, S. Lü, X. Meng, Y. Zhang, B. Yu, X. Li, Y. Sui, J. Yang, C. Fu and Y. Ji, Synthesis and characterization of $SmSrCo_{2-x}Mn_xO_{5+\delta}$ (x = 0.0, 0.2, 0.4, 0.6, 0.8, 1.0) cathode materials for intermediate-temperature solid-oxide fuel cells, *Ceram. Int.*, 2014, **40**, 11343–11350.
12 M. M. Natile, G. Eger, P. Batocchi, F. Mauvy and A. Glisenti, Strontium and copper doped $LaCoO_3$: new cathode materials for solid oxide fuel cells?, *Int. J. Hydrogen Energy*, 2017, **42**, 1724–1735.
13 S. W. Baek, J. H. Kim and J. Bae, Characteristics of ABO_3 and A_2BO_4 (A = Sm, Sr; B = Co, Fe, Ni) samarium oxide system as cathode materials for intermediate temperature-operating solid oxide fuel cell, *Solid State Ionics*, 2008, **179**, 1570–1574.
14 I. Fullarton, J. Jacobs and H. Van Benthem, Study of oxygen ion transport in acceptor doped samarium cobalt oxide, *Ionics*, 1995, **1**, 51–58.
15 J. Perez-Cacho, J. Blasco, J. Garcia and R. Sanchez, Relationships between Structure and Physical Properties in $SmNi_{1-x}Co_xO_3$, *J. Solid State Chem.*, 2000, **150**, 145–153.
16 H. Ullmann, N. Trofimenko, F. Tietz, D. Stöver and A. Ahmad-Khanlou, Correlation between thermal expansion and oxide ion transport in mixed conducting perovskite-type oxides for SOFC cathodes, *Solid State Ionics*, 2000, **138**, 79–90.
17 Y. Sun, W. Ren, S. Cao, H. Zhou, H. J. Zhao and H. Xu, Hydrostatic pressure driven spin, volume and band gap collapses in $SmFeO_3$: a GGA+U study, *Philos. Mag.*, 2016, **96**, 1613–1622.
18 H. J. Zhao, W. Ren, Y. Yang, X. M. Chen and L. Bellaiche, Effect of chemical and hydrostatic pressures on structural and magnetic properties of rare-earth orthoferrites: a first-principles study, *J. Phys.: Condens. Matter*, 2013, **25**, 466002.

19 S. Sahoo, P. K. Mahapatra and R. N. P. Choudhary, The structural, electrical and magnetoelectric properties of soft-chemically-synthesized $SmFeO_3$ ceramics, *J. Phys. D: Appl. Phys.*, 2016, **49**, 035302.

20 P. Ciambelli, S. Cimino, S. De Rossi, L. Lisi, G. Minelli, P. Porta and G. Russo, $AFeO_3$ (A = La, Nd, Sm) and $LaFe_{1-x}Mg_xO_3$ perovskites as methane combustion and CO oxidation catalysts: structural, redox and catalytic properties, *Appl. Catal., B*, 2001, **29**, 239–250.

21 R. Choithrani, N. K. Gaur and R. K. Singh, Thermodynamic properties of $SmMnO_3$, $Sm_{0.55}Sr_{0.45}MnO_3$ and $Ca_{0.85}Sm_{0.15}MnO_3$, *J. Phys.: Condens. Matter*, 2008, **20**, 415201.

22 W. Lee, J. W. Han, Y. Chen, Z. Cai and B. Yildiz, Cation size mismatch and charge interactions drive dopant segregation at the surfaces of manganite perovskites, *J. Am. Chem. Soc.*, 2013, **135**, 7909–7925.

23 N. Shukla, T. Joshi, S. Dasgupta, P. Borisov, D. Lederman and S. Datta, Electrically induced insulator to metal transition in epitaxial $SmNiO_3$ thin films, *Appl. Phys. Lett.*, 2014, **105**, 2012–2017.

24 I. V. Nikulin, M. A. Novojilov, A. R. Kaul, S. N. Mudretsova and S. V. Kondrashov, Oxygen nonstoichiometry of N_dNiO_{3-d} and $SmNiO_{3-d}$, *Mater. Res. Bull.*, 2004, **39**, 775–791.

25 R. Pelosato, G. Cordaro, D. Stucchi, C. Cristiani and G. Dotelli, Cobalt based layered perovskites as cathode material for intermediate temperature solid oxide fuel cells: a brief review, *J. Power Sources*, 2015, **298**, 46–67.

26 M. Karppinen, H. Yamauchi, H. Suematsu, K. Isawa, M. Nagano, R. Itti and O. Fukunaga, Control on the Copper Valence and Properties by Oxygen Content Adjustment in the $LaCuO_{3-y}$ System ($0 \leq y \leq 0.5$), *J. Solid State Chem.*, 1997, **130**, 213–222.

27 M. Karppinen, H. Yamauchi, T. Ito, H. Suematsu and O. Fukunaga, High-pressure synthesis and thermal decomposition of $LaCuO_3$, *Mater. Sci. Eng., B*, 1996, **41**, 59–62.

28 J. Perez-Cacho, J. Blasco, J. Garcia, M. Castro, J. Stankiewicz, M. C. Sanchez and R. D. Sanches, Magnetic Properties of $SmNiO_3$, *J. Magn. Magn. Mater.*, 1999, **196–197**, 541.

29 A. Gupta, B. Mercey, H. Hervieu and B. Raveau, Thin-Film Stabilization of Metastable Phases in the $Sm_{1-x}Sr_xCuO_y$ System, *Chem. Mater.*, 1994, **6**, 1011–1016.

30 N. J. C. Ingle, R. H. Hammond and M. R. Beasley, Molecular beam epitaxial growth of $SrCu_2O_3$: metastable structures and the role of epitaxy, *J. Appl. Phys.*, 2002, **91**, 6371.

31 G. Kresse and J. Hafner, *Ab initio* molecular dynamics for liquid metals, *Phys. Rev. B: Condens. Matter Mater. Phys.*, 1993, **47**, 558.

32 G. Kresse and J. Hafner, *Ab initio* molecular-dynamics simulation of the liquid-metal–amorphous-semiconductor transition in germanium, *Phys. Rev. B: Condens. Matter Mater. Phys.*, 1994, **49**, 14251.

33 G. Kresse and J. Furthmüller, Efficiency of *ab initio* total energy calculations for metals and semiconductors using a plane-wave basis set, *Comput. Mater. Sci.*, 1996, **6**, 15–50.

34 G. Kresse and J. Furthmüller, Efficient iterative schemes for *Ab initio* total-energy calculations using a plane-wave basis set, *Phys. Rev. B: Condens. Matter Mater. Phys.*, 1996, **54**, 11169–11186.

35 P. E. Blöchl, Projector augmented-wave method, *Phys. Rev. B: Condens. Matter Mater. Phys.*, 1994, **50**, 17953.

36 J. Perdew, K. Burke and M. Ernzerhof, Errata: Generalized Gradient Approximation Made Simple, *Phys. Rev. Lett.*, 1996, **77**, 1396.

37 J. Perdew, K. Burke and M. Ernzerhof, Errata: Generalized Gradient Approximation Made Simple, *Phys. Rev. Lett.*, 1997, **78**, 1396.

38 P. E. Blöchl, O. Jepsen and O. K. Andersen, Improved tetrahedron method for Brillouin-zone integrations, *Phys. Rev. B: Condens. Matter Mater. Phys.*, 1994, **49**, 16223–16233.

39 H. J. Monkhorst and J. D. Pack, Special points for Brillouin-zone integrations, *Phys. Rev. B: Solid State*, 1976, **13**, 5188–5192.

40 R. F. W. Bader, *Atoms in Molecules: A Quantum Theory*, Oxford University Press, Oxford, 1990.

41 G. Henkelman, A. Arnaldsson and H. Jónsson, A fast and robust algorithm for Bader decomposition of charge density, *Comput. Mater. Sci.*, 2006, **36**, 354–360.

42 T. Geng, Z. Han and S. Zhuang, Effective Coulomb interaction in $LaMnO_3$, *Phys. B*, 2010, **405**, 3714–3716.

43 P. Ravindran, A. Kjekshus, H. Fjellvåg, A. Delin and O. Eriksson, Ground-state and excited-state properties of $LaMnO_3$ from full-potential calculations, *Phys. Rev. B: Condens. Matter Mater. Phys.*, 2002, **65**, 064445.

44 P. Ravindran, R. Vidya, H. Fjellvåg and A. Kjekshus, Electronic Structure and Excited-state Properties of Perovskite-like Oxides, *J. Cryst. Growth*, 2004, **268**, 554–559.

45 S. Dudarev, G. Botton and S. Savrasov, Electron-energy-loss spectra and the structural stability of nickel oxide: an LSDA+U study, *Phys. Rev. B: Condens. Matter Mater. Phys.*, 1998, **57**, 1505–1509.

46 Y.-L. Lee, J. Kleis, J. Rossmeisl and D. Morgan, *Ab initio* energetics of $LaBO_3$(001) (B = Mn, Fe, Co, and Ni) for solid oxide fuel cell cathodes, *Phys. Rev. B: Condens. Matter Mater. Phys.*, 2009, **80**, 224101.

47 A. M. Ritzmann, J. M. Dieterich and E. A. Carter, DFT+U analysis of the electronic structure and defect chemistry of LSCF, *Phys. Chem. Chem. Phys.*, 2016, **18**, 12260–12269.

48 E. Olsson, X. Aparicio-Anglès and N. H. de Leeuw, *Ab initio* study of vacancy formation in cubic $LaMnO_3$ and $SmCoO_3$ as cathode materials in solid oxide fuel cells, *J. Chem. Phys.*, 2016, **145**, 014703.

49 S. Vázquez, L. Suescun and R. Faccio, Effect of Cu doping on $Ba_{0.5}Sr_{0.5}Fe_{1-x}Cu_xO_{3-\delta}$ perovskites for solid oxide fuel cells: a first-principles study, *J. Power Sources*, 2016, **311**, 13–20.

50 S. Fares, Frequency dependence of the electrical conductivity and dielectric constants of polycarbonate (Makrofol-E) film under the effects of γ-radiation, *Nat. Sci.*, 2011, **03**, 1034–1039.

51 M. Mehedi Hassan, A. S. Ahmed, M. Chaman, W. Khan, A. H. Naqvi and A. Azam, Structural and frequency dependent dielectric properties of Fe^{3+} doped ZnO nanoparticles, *Mater. Res. Bull.*, 2012, **47**, 3952–3958.

52 M. Gajdoš, K. Hummer, G. Kresse, J. Furthmüller and F. Bechstedt, Linear optical properties in the projector-augmented wave methodology, *Phys. Rev. B: Condens. Matter Mater. Phys.*, 2006, **73**, 1–9.

53 J. D. Baran, M. Molinari, N. Kulwongwit, F. Azough, R. Freer, D. Kepaptsoglou, Q. M. Ramasse and S. C. Parker, Tuning Thermoelectric Properties of Misfit Layered Cobaltites by Chemically Induced Strain, *J. Phys. Chem. C*, 2015, **119**, 21818–21827.

54 I. T. Todorov, W. Smith, K. Trachenko and M. T. Dove, DL_POLY, *J. Mater. Chem.*, 2006, **16**, 1911–1918.

55 W. G. Hoover, Canonical dynamics: equilibrium phase-space distributions, *Phys. Rev. A: At., Mol., Opt. Phys.*, 1985, **31**, 1695–1697.

56 M. Born and J. Mayer, Lattice theory of ionic solids, *Phys. B*, 1932, **75**, 1–18.

57 J. E. Mayer, Dispersion and Polarizability and the van der Waals Potential in the Alkali Halides, *J. Chem. Phys.*, 1933, **1**, 270–279.

58 M. S. Islam, M. Cherry and C. R. A. Catlow, Oxygen Diffusion in $LaMnO_3$ and $LaCoO_3$ Perovskite-Type Oxides: A Molecular Dynamics Study, *J. Solid State Chem.*, 1996, **124**, 230–237.

59 M. A. Farhan and M. J. Akhtar, Negative pressure driven phase transformation in Sr doped $SmCoO_3$, *J. Phys.: Condens. Matter*, 2010, **22**, 075402.

60 M. Cherry, M. S. Islam and C. R. A. Catlow, Oxygen ion migration in perovskite-type oxides, *J. Solid State Chem.*, 1995, **118**, 125–132.

61 E. Olsson, X. Aparicio-Anglès and N. H. de Leeuw, A computational study of the electronic properties, ionic conduction, and thermal expansion of $Sm_{1-x}A_xCoO_3$ and $Sm_{1-x}A_xCoO_{3-x/2}$ (A = Ba^{2+}, Ca^{2+}, Sr^{2+}, and x = 0.25, 0.5) as intermediate temperature SOFC cathodes, *Phys. Chem. Chem. Phys.*, 2017, **19**, 13960–13969.

62 R. Grau-Crespo, S. Hamad, C. R. A. Catlow and N. H. de Leeuw, Symmetry-adapted configurational modelling of fractional site occupancy in solids, *J. Phys.: Condens. Matter*, 2007, **19**, 256201.

63 T. N. Vasil'chikova, T. G. Kuz'mova, A. A. Kamenev, A. R. Kaul' and A. N. Vasil'ev, Spin states of cobalt and the thermodynamics of $Sm_{1-x}Ca_xCoO_{3-\delta}$ solid solutions, *JETP Lett.*, 2013, **97**, 34–37.

64 E. Olsson, X. Aparicio-Anglès and N. H. de Leeuw, A DFT+U study of the structural, electronic, magnetic, and mechanical properties of cubic and orthorhombic $SmCoO_3$, *J. Chem. Phys.*, 2016, **145**, 224704.

65 T. Arima and Y. Tokura, Optical Study of Electronic Structure in Perovskite-Type RMO_3 (R = La, Y; M = Sc, Ti, V, Cr, Mn, Fe, Co, Ni, Cu), *J. Phys. Soc. Jpn.*, 1995, **64**, 2488–2501.

66 H. Y. Lee, K. Huang and J. B. Goodenough, Sr- and Ni-Doped $LaCoO_3$ and $LaFeO_3$ Perovskites, *J. Electrochem. Soc.*, 1998, **145**, 3220–3227.

67 I. Loa, P. Adler, A. Grzechnik, K. Syassen, U. Schwarz, M. Hanfland, G. Rozenberg, P. Gorodetsky and M. P. Pasternak, Pressure-induced quenching of the Jahn-Teller distortion and insulator-to-metal transition in $LaMnO_3$, *Phys. Rev. Lett.*, 2001, **87**, 125501.

68 M. Pavone, A. B. Muñoz-Garcia, A. M. Ritzmann and E. A. Carter, First-Principles Study of Lanthanum Strontium Manganite: new Insights into Electronic Structure and Oxygen Vacancy Formation, *J. Phys. Chem. C*, 2014, **118**, 13346–13356.

69 J. H. Park, S. Cheong and C. T. Chen, Double-exchange ferromagnetism in $La(Mn_{1-x}Co_xO)_3$, *Phys. Rev. B: Condens. Matter Mater. Phys.*, 1997, **55**, 11072–11075.

70 W. Zhou, R. Ran and Z. Shao, Progress in understanding and development of $Ba_{0.5}Sr_{0.5}Co_{0.8}Fe_{0.2}O_{3-\delta}$-based cathodes for intermediate-temperature solid-oxide fuel cells: a review, *J. Power Sources*, 2009, **192**, 231–246.

71 L. W. Tai, M. M. Nasrallah, H. U. Anderson, D. M. Sparlin and S. R. Sehlin, Structure and electrical properties of $La_{1-x}Sr_xCo_{1-y}Fe_yO_3$. Part 2. The system $La_{1-x}Sr_xCo_{0.2}Fe_{0.8}O_3$, *Solid State Ionics*, 1995, **76**, 273–283.

72 J. Richter, P. Holtappels, T. Graule, T. Nakamura and L. J. Gauckler, Materials design for perovskite SOFC cathodes, *Monatsh. Chem.*, 2009, **140**, 985–999.

73 L. W. Tai, M. M. Nasrallah, H. U. Anderson, D. M. Sparlin and S. R. Sehlin, Structure and electrical properties of $La_{1-x}Sr_xCo_{1-y}Fe_yO_3$. Part 1. The system $La_{0.8}Sr_{0.2}Co_{1-y}Fe_yO_3$, *Solid State Ionics*, 1995, **76**, 259–271.

74 J. Mizusaki, N. Mori, H. Takai and Y. Yonemura, Oxygen nonstoichiometry and defect equilibrium in the perovskite-type oxides $La_{1-x}Sr_xMnO_{3+d}$, *Solid State Ionics*, 2000, **129**, 163–177.

75 J. Mizusaki and Y. Miwa, Nonstoichiometry of the Perovskite-Type Oxides $La_{1-x}Sr_xCoO_{3-d}$, *J. Solid State Chem.*, 1989, **80**, 102–111.

76 R. Scurtu, S. Somacescu, J. M. Calderon-Moreno, D. Culita, I. Bulimestru, N. Popa, A. Gulea and P. Osiceanu, Nanocrystalline $Sm_{0.5}Sr_{0.5}CoO_{3-\delta}$ synthesized using a chelating route for use in IT-SOFC cathodes: microstructure, surface chemistry and electrical conductivity, *J. Solid State Chem.*, 2014, **210**, 53–59.

77 C. Sun, R. Hui and J. Roller, Cathode materials for solid oxide fuel cells: a review, *J. Solid State Electrochem.*, 2009, **14**, 1125–1144.

78 P. Erhart, A. Klein, D. Åberg and B. Sadigh, Efficacy of the DFT+U formalism for modeling hole polarons in perovskite oxides, *Phys. Rev. B: Condens. Matter Mater. Phys.*, 2014, **90**, 1–8.

79 S. Zhang and J. Northrup, Chemical potential dependence of defect formation energies in GaAs: application to Ga self-diffusion, *Phys. Rev. Lett.*, 1991, **67**, 2339–2342.

80 H. Raebiger, S. Lany and A. Zunger, Origins of the p-type nature and cation deficiency in Cu_2O and related materials, *Phys. Rev. B: Condens. Matter Mater. Phys.*, 2007, **76**, 045209.

81 T. Tanaka, K. Matsunaga, Y. Ikuhara and T. Yamamoto, First-principles study on structures and energetics of intrinsic vacancies in $SrTiO_3$, *Phys. Rev. B: Condens. Matter Mater. Phys.*, 2003, **68**, 205213.

82 C. G. Van De Walle and J. Neugebauer, First-principles calculations for defects and impurities: applications to III-nitrides, *J. Appl. Phys.*, 2004, **95**, 3851–3879.

83 P. G. Sundell, M. E. Björketun and G. Wahnström, Thermodynamics of doping and vacancy formation in $BaZrO_3$ perovskite oxide from density functional calculations, *Phys. Rev. B: Condens. Matter Mater. Phys.*, 2006, **73**, 104112.

84 A. M. Ritzmann, M. Pavone, A. B. Muñoz-García, J. A. Keith and E. A. Carter, *Ab initio* DFT+U analysis of oxygen transport in $LaCoO_3$: the effect of Co^{3+} magnetic states, *J. Mater. Chem. A*, 2014, **2**, 8060–8074.

85 C. Persson, Y. J. Zhao, S. Lany and A. Zunger, n-Type doping of $CuInSe_2$ and $CuGaSe_2$, *Phys. Rev. B: Condens. Matter Mater. Phys.*, 2005, **72**, 1–14.

86 E. Pawlas-Foryst, K. T. Jacob and K. Fitzner, Thermodynamics of $SmMnO_3$ and $SmMn_2O_5$ Phases Determined by the E. M. F. Method, *Arch. Metall. Mater.*, 2006, **51**, 253–260.

87 S. C. Parida, V. Venugopal and K. T. Jacob, Thermodynamic properties of $SmFeO_3$(s) and $Sm_3Fe_5O_{12}$(s), *J. Phase Equilib.*, 2003, **24**, 431–440.

88 Q. Li, Y.-X. Deng, Y.-A. Zhu, Y. Li, Z.-J. Sui, D. Chen and W.-K. Yuan, Structural stability of lanthanum-based oxygen-deficient perovskites in redox catalysis: a density functional theory study, *Catal. Today*, 2018, DOI: 10.1016/j.cattod.2018.04.070.

89 A. M. Ritzmann and A. B. Muñoz-García, *Ab initio* DFT+U Analysis of Oxygen Vacancy Formation and Migration in $La_{1-x}Sr_xFeO_{3-\delta}$ (x = 0, 0.25, 0.50), *Chem. Mater.*, 2013, **25**, 3011–3019.